From Causal Auditing to Value Maximization: Individualized Management Guidelines for Offshore Wind Assets

Yi Zeng

Abstract—The current offshore wind asset management paradigm is plagued by the "Population Fallacy", heavily relying on unified alarm thresholds and periodic maintenance strategies. This "one-size-fits-all" model inevitably leads to severe economic inefficiencies: healthy assets are prematurely retired, while sub-healthy assets frequently suffer sudden catastrophic failures. This paper proposes the final evolutionary form of the "Clark Paradigm"—a top-level guideline aimed at achieving individualized asset management and economic value maximization, ultimately engineered into the "Bianque System". Adhering to the preventive philosophy of "treating the disease before it occurs" in classical Chinese medicine, and taking the inherent 0.3% material deviation in high-precision manufacturing as the electromagnetic "digital fingerprint", this guideline advocates establishing a dynamic "Individualized Health Ledger" for each wind turbine. We propose a paradigm shift from static electromagnetic feature auditing to dynamic fault contagion tracking, arguing that the retirement red line should no longer be defined by design life, but by monitoring the convergence of the "fault contagion cycle" to draw an absolute "economic boundary". Relying on data-driven precise economic inputs and dynamic derating strategies, the "Bianque System" constructs an implementation framework to squeeze the maximum residual value out of offshore wind turbines, fundamentally transforming traditional Operation & Maintenance (O&M) from a passive "cost center" into a predictive "value creation center".

Index Terms—Asset value maximization, Causal auditing, Individualized health ledger, Offshore wind farm, Predictive maintenance, Multi-terminal harmonic fingerprints.

I. Introduction: The "Population Fallacy" and Paradigm Crisis

WITH the acceleration of the global energy transition, offshore wind power is advancing towards deep and far-sea areas. However, the complex marine environment and high dispatch costs have led to a sharp increase in operation and maintenance (O&M) expenditures, severely threatening the competitiveness of the Levelized Cost of Energy (LCOE) [1]–[5]. Currently, the industry generally adopts a management model of periodic maintenance and unified alarm thresholds—which this paper defines as the "Population Fallacy" [6]–[10].

This "one-size-fits-all" standard assumes that equipment of the same model and within the same wind farm follows identical degradation trajectories. In reliability engineering and asset management practices, this "Population Fallacy" is concentrated in three aspects:

1) Time Averaging Fallacy: Adopting the Mean Time Between Failures (MTBF) based on statistical averages as a predictive indicator for individual wind turbines. However, the aging of a single device is determined by the dynamic environmental loads it experiences in real time; static time averages cannot reflect an individual's current degradation slope.
2) Spatial Averaging Fallacy: Assuming all wind turbines within the same wind farm are subjected to the same stress states. In reality, due to wind-wave shear, wake effects, and geographical microclimate differences, the fatigue loads experienced by turbines at the core versus the periphery of a wind farm differ by orders of magnitude.
3) Manufacturing Consistency Assumption Fallacy: Ignoring micro-tolerances during the manufacturing and assembly of high-precision equipment. Even generators or converters of the same batch from the same assembly line exhibit approximately 0.3% deviations in material and electromagnetic geometric structures.

The economic cost of this population fallacy is immense: on one hand, healthy wind turbines undergo unnecessary interventions and early retirement, wasting substantial useful life and capital expenditure; on the other hand, sub-healthy turbines often experience severe failures before the next scheduled inspection, leading to exorbitant emergency hoisting costs, delayed spare parts logistics, and incalculable downtime losses.

In traditional Preventive Maintenance (PM) and Reliability-Centered Maintenance (RCM) research, Optimal Stopping Theory is often utilized to find the best time for equipment replacement under uncertain environments. However, existing academic outcomes and industrial practices generally assume that equipment operates in isolation, ignoring the fault contagion inherent in complex transmission and distribution network topologies. In an offshore wind farm, a sub-healthy harmonic distortion or partial discharge anomaly in one device will rapidly propagate through the submarine cable network to adjacent wind turbines, accelerating the insulation degradation of surrounding healthy turbines, thereby triggering cascading failures.

To break the industry's "one-size-fits-all" stereotype, the "Clark Paradigm" has constructed a solid physical causal diagnostic theory: First, it utilizes multi-terminal harmonic fingerprints for causal auditing, establishing the static electromagnetic characterization of individualized assets [11]; Second, by tracking the transient propagation delay (ΔT) of precursor signals among topological nodes, it achieves dynamic causal tracking and precise source localization of sub-healthy precursors [12]; Third, it constructs a multi-terminal spatio-temporal fault contagion topology model, realizing the trajectory tracking and quantitative evolutionary modeling of faults in the transmission and distribution network [13].

However, the existing physical and diagnostic frameworks have yet to directly answer the core questions at the commercial operation level: How to translate microscopic physical features into optimal economic decisions? How to determine the best equilibrium point for replacing components to squeeze the ultimate residual value over the full life cycle?

This paper aims to complete the final Paradigm Shift towards "economy and value". We transform the aforementioned physical causal theory into concrete guidelines for maximizing economic benefits, and formally propose the "Bianque System". Just as the supreme realm of medicine praised by the ancient Chinese physician Bianque—"superior doctors prevent the disease"—the core mission of the "Bianque System" is by no means expensive rescues after the asset is completely destroyed, but rather, during the sub-healthy state or even earlier microscopic deviation stages, to achieve the ultimate extraction of capital economic benefits by tracking and blocking fault contagion. The core contributions of this paper include:

1) We propose a physical-economic cross-scale causal mapping theory that links micro electromagnetic features with macro asset expected value.
2) We reshape the definition of asset health and propose a "dual red line mechanism" based on Optimal Stopping Theory to formally solve for the optimal downtime.
3) For fault contagion in electrical topology networks, we perform a rigorous derivation of graph dynamics stability and use an implicit finite difference method to numerically solve the Partial Integro-Differential Equation (PIDE) for the optimal stopping boundary.
4) We discuss the thermomechanical stress degradation relationship under asset derating operations and adopt a grid-connected damping stability control reconstruction algorithm to achieve "squeezing residual value without polluting the grid."
5) We propose a non-productized, bespoke enterprise-level software implementation framework to achieve deep decoupling and flexible configuration between health ledger data and the asset owner's specific business logic.

II. Paradigm Foundation: Theoretical Foundation of Multi-dimensional Causal Networks

The transition to individualized economic management is built upon the physical causal mapping theory constructed by the Clark Paradigm. To establish a clear spatio-temporal topological representation, the theory divides the offshore wind power transmission chain into five critical physical nodes: Generator (Node A), Converter (Node B), Unit Box Transformer (Node C), Collector Submarine Cable (Node D), and Offshore Substation / Grid PCC (Node E). Considering the physical span and high-frequency attenuation of the transmission path, Node C and Node D are further subdivided into two monitoring points: the low-voltage and medium-voltage monitoring points on the transformer side (C_1, C_2), and the sending and receiving ends of the submarine cable (D_1, D_2). These five nodes and their corresponding subdivided monitoring points together constitute the physical boundary of the multi-terminal causal network, providing the underlying scientific and technological support for this guideline.

A. Electromagnetic Feature Auditing and Mathematical Characterization Based on 0.3% Inherent Material Deviation

No two high-precision power devices and transmission lines are completely identical. Manufacturing tolerances such as flux density variations, air-gap eccentricity, or microscopic irregularities of cable conductors result in an inherent physical difference of approximately 0.3% in assets. This subtle deviation serves precisely as the unique "electromagnetic fingerprint feature" for each asset node (Node A to E). Here, the mathematical and physical connotations of the five key nodes are defined in detail:

1) Node A (Generator): The generator is the originating source of the conversion from mechanical energy to electrical energy. Its stator-rotor eccentricity and non-uniform winding distribution directly modulate the air-gap permeance distribution. Let the pole pairs of the generator be p, the stator power frequency angular frequency be ω_s, and the rotor mechanical rotation angular frequency be ω_r. When local insulation degradation occurs in the stator winding due to overload operation, its local leakage inductance L_{sl} and stator impedance deviate asymmetrically, thereby affecting the electromagnetic transient reactance. The equivalent sub-transient reactance X_d'' of the generator during the sub-transient process can be approximately expressed as:

$$X_d'' \approx X_a + \frac{X_f X_{kd}}{X_f + X_{kd}} \tag{1}$$

where X_a is the stator leakage reactance, X_f is the excitation winding reactance, and X_{kd} is the equivalent damper winding reactance. Microscopic stator insulation degradation leads to the drift of X_a, which is directly reflected in the transient characteristics of the output current. The mapping relationship between the aging degree and the degradation of the sub-transient reactance is shown in Fig. 2.

When rotor eccentricity occurs, the air-gap permeance is dynamically modulated along the spatial angle θ and time t. At this time, the modulation of the air-gap flux density $B(\theta, t)$ can be characterized as:

$$B(\theta, t) = B_m \cos(p\theta - \omega_s t)\,[1 + \epsilon \cos(\theta - \omega_r t)] \tag{2}$$

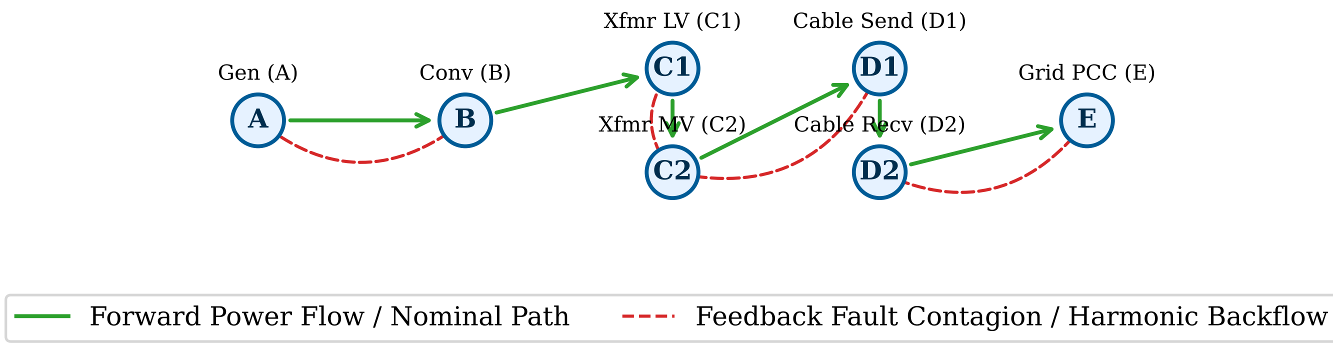

Fig. 1. Schematic diagram of the interactive relationship between the physical power transmission topology and the multi-terminal fault contagion/feedback topology based on nodes A–E.

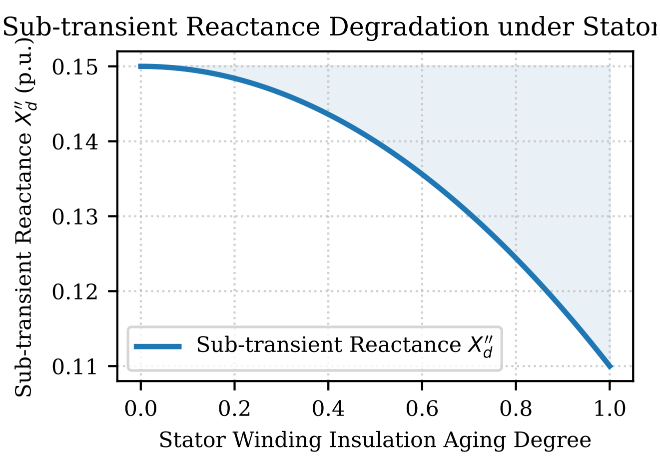

Fig. 2. Simulation mapping curve of the relation between stator winding insulation aging degree and generator equivalent sub-transient reactance X_d'' degradation.

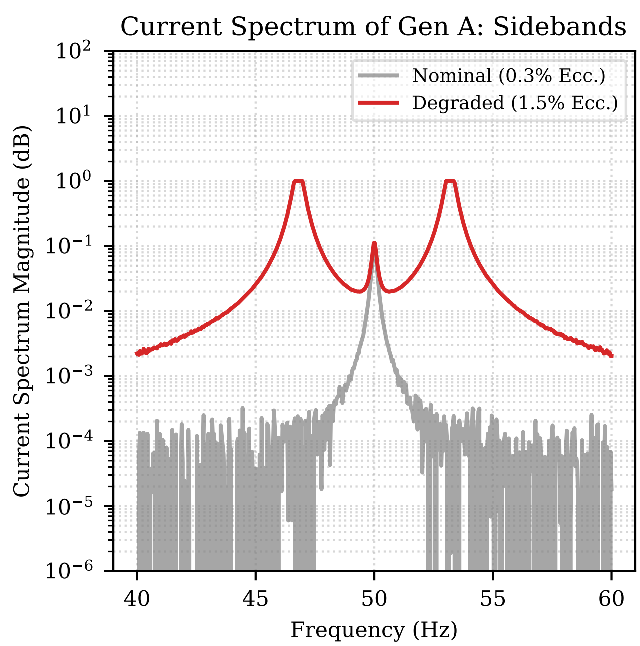

Fig. 3. Comparison of frequency-domain sideband harmonic spectra of stator output current of Generator A under high-precision electromagnetic fingerprint (0.3% eccentricity) and degraded eccentricity (1.5% eccentricity).

where ϵ is the eccentricity coefficient. The stator winding cuts this modulated magnetic field, exciting specific sideband frequency components in the stator current $i_A(t)$:

$$\begin{aligned} i_A(t) = & I_0 \cos(2\pi f_s t + \phi_0) \\ & + \sum_{k=1}^{K} I_k \cos(2\pi(f_s \pm k f_r)t + \phi_{\pm k}) \end{aligned} \tag{3}$$

These low-frequency envelope harmonic amplitudes I_k accompanying the rotational frequency eccentricity modulation constitute the characteristic fingerprint of the generator's eccentric wear [14]–[16]. The comparison of the simulated transient spectral deviation is shown in Fig. 3.

2) Node B (Converter): The converter consists of high-frequency IGBT switches and an LCL filter. The natural resonance frequency of the LCL filter at the converter outlet is:

$$f_{res} = \frac{1}{2\pi}\sqrt{\frac{L_{inv} + L_{grid}}{L_{inv} L_{grid} C_f}} \tag{4}$$

where L_{inv} and L_{grid} are the inverter-side and grid-side filter inductances, respectively, and C_f is the filter capacitance. In actual operation, the metallized self-healing effect of the filter capacitor C_f causes its capacity to decline slowly. When C_f undergoes a 20% capacitance deviation, the resonance frequency f_{res} will drift toward high frequencies. This easily overlaps with the closed-loop control bandwidth of the converter, triggering control loop instability and resonance outbreak [17]–[19]. The effect of filter capacitor degradation on the LCL resonance frequency is shown in Fig. 4.

Its fingerprint depends simultaneously on the PWM switching dead-time effect and the conduction impedance of the power semiconductors. The waveform distortion voltage $\Delta v_B(t)$ introduced by the dead-time t_d can be

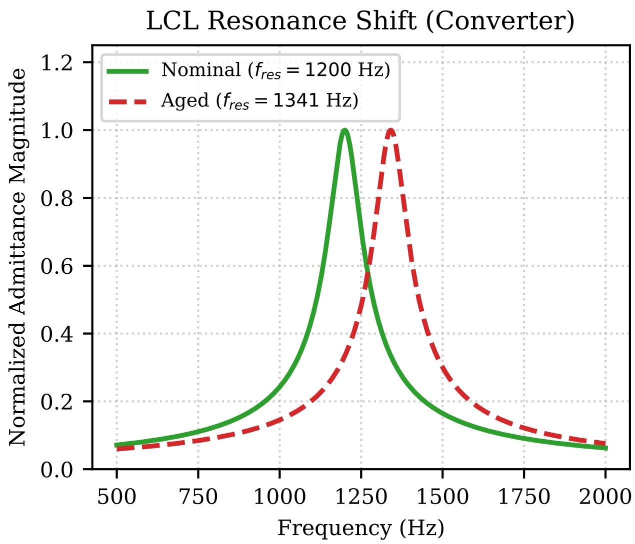

Fig. 4. Resonant frequency shift curves of the equivalent admittance at the outlet of Converter B due to capacitor C_f degradation.

expanded by Fourier series:

$$\Delta v_B(t) = \frac{4}{\pi} V_{dc} \sum_{n=1,3,5..}^{\infty} \left[\frac{1}{n} - \frac{2 f_{sw} t_d}{n} \right] \cdot \sin(n\omega_s t) \tag{5}$$

where V_{dc} is the DC-side voltage, and f_{sw} is the switching frequency. The transfer function of the phase dynamic deviation $\Delta\theta_{PLL}(s)$ of the Phase-Locked Loop (PLL) under grid-side voltage perturbation is:

$$H_{PLL}(s) = \frac{\Delta\theta_{PLL}(s)}{\Delta\theta_{grid}(s)} = \frac{K_p s + K_i}{s^2 + K_p s + K_i} \tag{6}$$

where K_p and K_i are the proportional and integral coefficients of the PLL PI regulator, respectively. This determines the transient response characteristics of the PLL to micro-tuning of impedance.

3) Node C (Unit Box Transformer): The magnetic core saturation characteristics of transformers exhibit high individual differences. When their excitation flux enters the saturation region, the excitation current $i_{C,mag}(t)$ can be expanded in odd harmonics [20]–[22]:

$$i_{C,mag}(t) = I_1 \sin(\omega_s t) + I_3 \sin(3\omega_s t + \psi_3) + I_5 \sin(5\omega_s t + \psi_5) \tag{7}$$

For transformer insulation systems, aging and moisture under thermo-electric stress cause the dielectric loss factor $\tan\delta$ to increase, and the equivalent insulation loss power can be characterized as:

$$P_d = \omega_s C_{ins} V^2 \tan\delta \tag{8}$$

where C_{ins} is the equivalent capacitance between windings or between winding and ground. With the drift of the dielectric loss factor, the fingerprint of the transformer's high-frequency excitation admittance will undergo measurable changes. Fig. 5 illustrates the comparison of nonlinear magnetization characteristics under magnetic core polarity degradation of the box transformer.

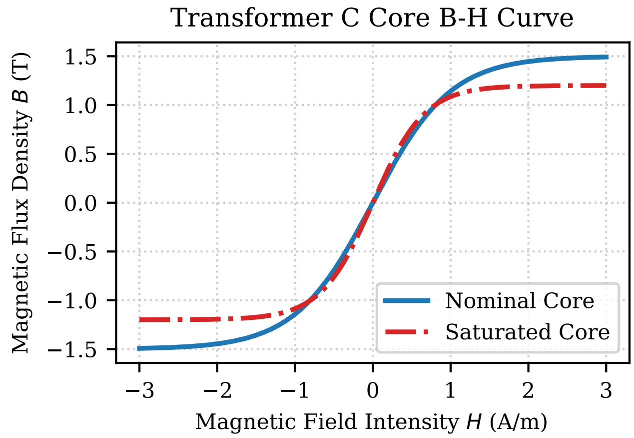

Fig. 5. Comparison of B-H hysteresis loop degradation simulation under magnetic saturation of Transformer C.

The ferromagnetic saturation characteristic of the transformer is nonlinear. Under the action of its nonlinear excitation characteristics, a characteristic transient magnetic relaxation delay is established between the low-voltage side C_1 input and the medium-voltage side C_2 output due to the dynamic response of the leakage inductance L_{leak} and winding resistance R_{wind}:

$$\tau_{mag} \approx \frac{L_{leak}}{R_{wind}} \tag{9}$$

This transient delay is a key causal variable for diagnosing transformer winding displacement and core deformation.

4) Node D (Collector Submarine Cable): Submarine cables are electromagnetic wave impedance transmission media determined by distributed parameters. Under high-frequency harmonics, due to the combined action of the skin effect and the proximity effect, the equivalent AC resistance $R_{ac}(f)$ of the submarine cable increases significantly:

$$R_{ac}(f) = R_{dc}\,(1 + y_s + y_p) \tag{10}$$

where y_s is the skin effect factor, and y_p is the proximity effect factor. At the 35th and higher harmonics, R_{ac} can reach 5 to 10 times the DC resistance. This causes local harmonic current anomalies to generate intense heat accumulation at the physical degradation location of the cable [23], [24]. The relationship between the AC/DC resistance ratio and frequency at high frequencies is shown in Fig. 6.

Let the resistance, inductance, capacitance, and conductance per unit length be R, L, C, and G, respectively. The two-port network characteristics of traveling waves in the

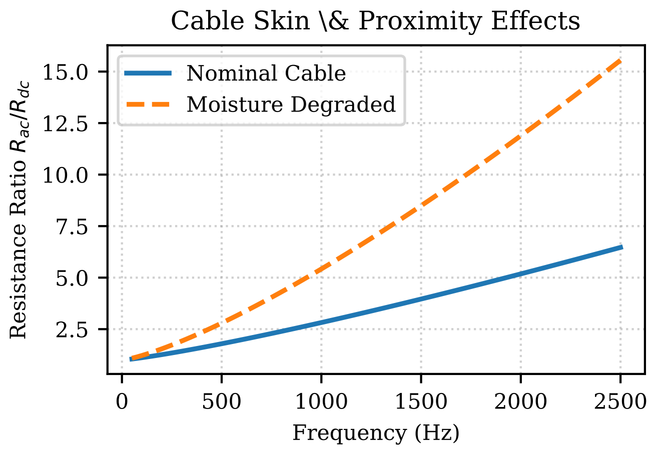

Fig. 6. Comparison of equivalent AC resistance increment ratio under nominal state and insulation moisture state of collector submarine cable D.

submarine cable satisfy the following frequency-domain telegrapher's state equations:

$$\begin{bmatrix} V_{D2}(\omega) \\ I_{D2}(\omega) \end{bmatrix} = \begin{bmatrix} \cosh(\gamma l) & -Z_c \sinh(\gamma l) \\ -\frac{1}{Z_c}\sinh(\gamma l) & \cosh(\gamma l) \end{bmatrix} \cdot \begin{bmatrix} V_{D1}(\omega) \\ I_{D1}(\omega) \end{bmatrix} \tag{11}$$

where l is the physical length of the submarine cable, $\gamma = \sqrt{(R + j\omega L)(G + j\omega C)}$ is the propagation constant, and $Z_c = \sqrt{\frac{R+j\omega L}{G+j\omega C}}$ is the characteristic impedance of the submarine cable. The physical transmission delay of high-frequency electromagnetic waves propagating from D_1 to D_2 is $\Delta T_D = l\sqrt{LC}$.

5) Node E (Offshore Substation / Grid PCC): This node is the vector convergence point of the grid-connected feeder harmonic currents. Assuming there are N grid-connected collector branches, the equivalent impedance network at the Point of Common Coupling (PCC) is:

$$Z_{PCC}(\omega) = Z_{grid}(\omega) \parallel \Big[\sum_{n=1}^{N} \big(Z_{cable,n}(\omega) + Z_{transformer,n}(\omega) \big)^{-1} \Big]^{-1} \tag{12}$$

The comprehensive harmonic current waveform injected by each unit into the PCC satisfies:

$$I_{PCC}(t) = \sum_{n=1}^{N} I_{feeder,n}(t - \Delta T_{path,n}) \tag{13}$$

where $\Delta T_{path,n}$ is the cumulative transmission delay from the n-th branch to the PCC.

B. Dynamic Causal Relationships based on Precursor Timing Tracking

On the basis of static fingerprints, dynamic causal relationships are introduced. As large-capacity electrical interconnection media, submarine cables exhibit typical broadband-dependent distributed inductance and capacitance due to the physical presence of their insulation layers (XLPE) and metallic shielding. When partial discharge (PD) or dielectric degradation precursors occur inside the submarine cable, dynamic changes in its microscopic relative permittivity ϵ_r will lead to micro-shifts in the propagation velocity $v_p = 1/\sqrt{LC}$. For typical XLPE-insulated submarine cables, the wave speed v_p usually ranges between 1.5×10^8 m/s and 2.0×10^8 m/s.

C. Multi-Terminal Spatio-Temporal Fault Contagion Topology Model and Graph Dynamics Stability Analysis

The wind farm collection network is abstracted as a directed graph $G = (V, E)$. Its topological structure is shown in Fig. 1. The forward and reverse fault contagion/harmonic feedback paths constitute the system's spatio-temporal causal topology [25]–[30].

The contagion evolution of the sub-health state of each node $i \in V$ is characterized by the following delayed differential equation:

$$\frac{dx_i(t)}{dt} = -\gamma_i x_i(t) + (1 - x_i(t)) \cdot \sum_{j \in \mathcal{N}_i} A_{ij}\beta_{ji}x_j(t - \Delta T_{ji}) \tag{14}$$

This delayed state transition process is known as the Contagion Network Delay Model (CNDM). To analyze the asymptotic stability of this spatio-temporal fault contagion network under dynamic operation, we construct the following Lyapunov-Krasovskii functional candidate [31]–[34]:

$$V(x_t) = \frac{1}{2}\sum_{i=1}^{N} x_i^2(t) + \sum_{i=1}^{N}\sum_{j\in\mathcal{N}_i}\int_{t-\Delta T_{ji}}^{t} x_j^2(s)ds \tag{15}$$

Taking the derivative of $V(x_t)$ along the system trajectories yields:

$$\dot{V}(x_t) = \sum_{i=1}^{N} x_i(t)\Big[-\gamma_i x_i(t) + (1 - x_i(t)) \cdot \sum_{j\in\mathcal{N}_i} A_{ij}\beta_{ji}x_j(t - \Delta T_{ji})\Big] + \sum_{i=1}^{N}\sum_{j\in\mathcal{N}_i}\left[x_j^2(t) - x_j^2(t - \Delta T_{ji})\right] \tag{16}$$

Using Young's inequality to scale the terms, the sufficient condition for system self-healing (i.e., fault contagion does not cause a global outbreak) is obtained: for all nodes i, the following must be satisfied:

$$\gamma_i > \frac{1}{2}\sum_{j\in\mathcal{N}_i} A_{ij}\beta_{ji}\left(1 + \Delta T_{ji}\right) \tag{17}$$

When Eq. (17) is satisfied under the current physical topology and derating state, the network is in the "self-healing stability region"; once this inequality is broken, fault contagion will spread through the topology at an exponential rate, at which point the second-track topological physical isolation mechanism must be triggered. The instantaneous diffusion convergence simulation of the system when the self-healing rate boundary is met is shown in Fig. 7. This demonstrates the necessity of graph topology reconstruction for cutting off cascading failures from a control theory perspective.

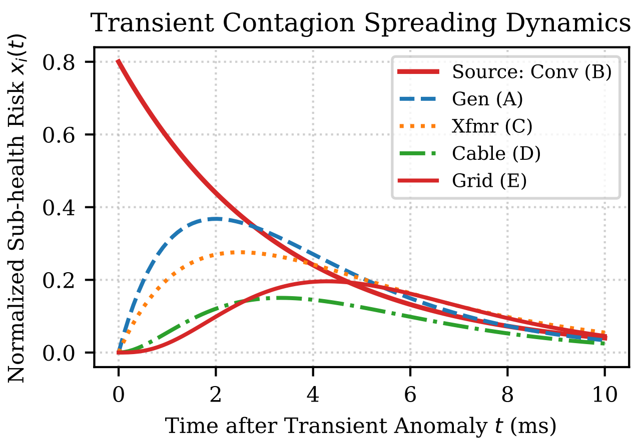

Fig. 7. Convergence evolution curves of degradation risk for topological nodes (A-E) in the fault contagion model when the self-healing criterion is met.

III. Core Guideline I: Establishing the "Individualized Health Ledger"

The industry monopoly of "unified standards" must be broken. One of the guidelines for electrical asset management in this paradigm is to establish a highly transparent "Individualized Health Ledger" for each heavy asset, analogous to the S.M.A.R.T. mechanism in the hard drive industry.

A. Redefining Asset Health

Under the Clark Paradigm, the absolute baseline of "health" must still strictly adhere to the physical red lines set by manufacturers and various industry specifications. However, the core of this paradigm is that this "baseline" must never be treated as the "passing grade" for management. Instead, health is redefined as a dynamic predictive deviation (Δ): the gap between the equipment's current Physical Reality and the Causal Expectation derived from its initial 0.3% fingerprint features.

To understand this concept more vividly, we can liken it to individual differences in clinical medicine: a marathon runner who has trained for a long time might have a resting heart rate of only 45 beats/min, which is typically diagnosed as "bradycardia" or even a pathological state in ordinary people, but for that individual, it is an excellent physiological balance point and health state. By the same token, for a wind turbine generator that inherently carries a 0.3% shaft eccentricity or specific harmonic deviation out of the factory due to manufacturing tolerances, traditional unified alarm thresholds will frequently trigger false alarms or fail to timely identify the degradation slope before a real fault occurs.

The core purpose of this reinvention is to predictively prevent catastrophic damage and cascading faults. Its significance is reflected in:

- First, eliminating the staggering collateral costs caused by unprepared passive downtime. In deep and far-sea environments, once a major component of a large-capacity wind turbine (e.g., generator stator winding, converter power module, submarine cable joint) suffers sudden burnout, the average passive downtime often lasts for months due to lengthy hoisting vessel scheduling, long spare parts procurement cycles, and extreme sea conditions hindering marine access. Performing preventive replacement at a planned economic point in time constitutes prepared rapid replacement, and the downtime losses become negligible.
- Second, cutting off the fault contagion chain to protect other healthy assets in the wind farm. In a complex electrical topology, a harmonic degradation anomaly in a single device will quickly inject harmonic stress into other grid-connected devices through the grid connection path, accelerating the insulation degradation of surrounding equipment. Severing the fault before it turns into catastrophic damage is an important means to protect the health of the entire wind farm grid.

B. Life-Cycle Five-Dimensional S.M.A.R.T. Auditing Mechanism

From the first day the equipment is connected to the grid to generate power, the individualized ledger begins recording its unique degradation curve. Whenever any harmonic parameter in the ledger shows an anomaly, the "Bianque System" will automatically generate a detailed auditing report for the user containing the following five dimensions:

1) Anomaly Marking and Physical Attribution: Precisely locating which frequency of harmonics exceeds the limit (e.g., H5 distortion) and marking the specific cause (e.g., rotor eccentricity or insulation aging).
2) Spatio-Temporal Impact Radius Assessment: Clarifying whether the anomaly only affects the device itself (Local), or will impact the entire line via collection cables (Line), or even cause harmonic pollution and backlash to upstream generators or downstream transformers.
3) Substantive Fault Prediction: Based on the feature base, accurately predicting which specific catastrophic faults this "sub-healthy" state will evolve into in the future.
4) Outbreak Timing (RUL) Prediction: Predicting the remaining time before the aforementioned substantive faults break out.

5) Economic Cost and Salvage Value Quantification: The system will clearly tell the user how much "salvage value" will be created if preventive measures are taken now.

C. Mathematical Reconstruction of the Individualized Health Index (IHI)

To comprehensively characterize the multi-terminal degradation trends of heterogeneous equipment in a single indicator, we define the Individualized Health Index $H(t)$:

$$H(t) = 1 - \sum_{k=1}^{K} w_k \cdot D_k(x_k(t)) \tag{18}$$

where $x_k(t)$ is the real-time measurement value of the k-th parameter in Table I, and $D_k(x_k(t)) \in [0, 1]$ is the corresponding normalized deviation function. For out-of-bounds indicators (like temperature, harmonic distortion rate):

$$D_k(x_k(t)) = \frac{|x_k(t) - x_{k,base}|}{x_{k,alarm} - x_{k,base}} \tag{19}$$

where $x_{k,base}$ is the exclusive 0.3% initial fingerprint baseline value for that asset, and $x_{k,alarm}$ is the industry red line threshold. The weight w_k is calculated using the entropy weight method, with the calculation steps as follows.

Construct a matrix $X = [x_{ik}]_{M\times K}$ containing M historical time samples and K measurement indicators, and normalize the indicators to obtain matrix $Y = [y_{ik}]_{M\times K}$, where:

$$y_{ik} = \frac{x_{ik} - \min_i x_{ik}}{\max_i x_{ik} - \min_i x_{ik}} \tag{20}$$

Calculate the proportion p_{ik} of each sample under indicator k:

$$p_{ik} = \frac{y_{ik}}{\sum_{i=1}^{M} y_{ik}} \tag{21}$$

Thereby calculate the information entropy e_k under the k-th indicator:

$$e_k = -\frac{1}{\ln M} \sum_{i=1}^{M} p_{ik} \ln p_{ik} \tag{22}$$

Calculate the difference coefficient $d_k = 1 - e_k$ according to the entropy value, and finally obtain the objective weight of each monitoring parameter:

$$w_k = \frac{d_k}{\sum_{j=1}^{K} d_j} \tag{23}$$

The calculated objective entropy weight distribution of the main operating parameters is shown in Fig. 8. This avoids the subjective bias of artificially setting weights and ensures the objective sensitivity of the health ledger to microscopic changes.

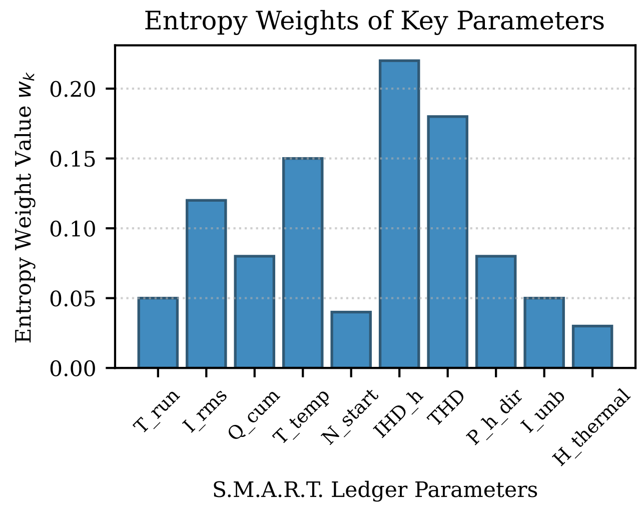

Fig. 8. Bar chart of objective weight distribution for core monitoring parameters calculated by the information entropy weight method.

D. Adaptive Baseline Calibration Algorithm for Individualized Feature Bases

During the initial stage of asset operation (e.g., the first 14 days of the "calibration window"), the "Bianque System" must establish the dynamic working condition baselines of specific equipment under different wind speeds and power outputs. To eliminate the interference of seasonal temperature variations and long-term external grid evolution on the 0.3% fingerprint features, we introduce the Recursive Least Squares with Forgetting Factor (RLS-FF) method to calibrate the feature baselines online in real time.

Let the observation model be $y(k) = \varphi^T(k)\theta_{base} + e(k)$, where $y(k)$ is the harmonic or temperature rise measurement vector, $\varphi(k)$ is the regression vector composed of real-time wind speed, output power, and ambient temperature, and θ_{base} is the baseline multi-dimensional fingerprint parameter to be calibrated. The recursive baseline update formulas are:

$$\begin{aligned} K(k) =& P(k-1)\varphi(k) \\ &\cdot \left[\lambda_{forget} + \varphi^T(k)P(k-1)\varphi(k)\right]^{-1} \end{aligned} \tag{24}$$

$$\begin{aligned} \theta_{base}(k) =& \theta_{base}(k-1) + K(k) \\ &\cdot \left[y(k) - \varphi^T(k)\theta_{base}(k-1)\right] \end{aligned} \tag{25}$$

$$\begin{aligned} P(k) =& \frac{1}{\lambda_{forget}}\Big[P(k-1) \\ &- K(k)\varphi^T(k)P(k-1)\Big] \end{aligned} \tag{26}$$

where $\lambda_{forget} \in [0.95, 0.99]$ is the forgetting factor, used to exponentially decay historical old data, allowing the individualized ledger baseline to adapt to long-term slow drift processes such as localized scouring along the submarine cable and natural aging of transformers. The online baseline correction process under overload perturbation noise interference is shown in Fig. 9, ensuring the continuous high sensitivity of causal analysis.

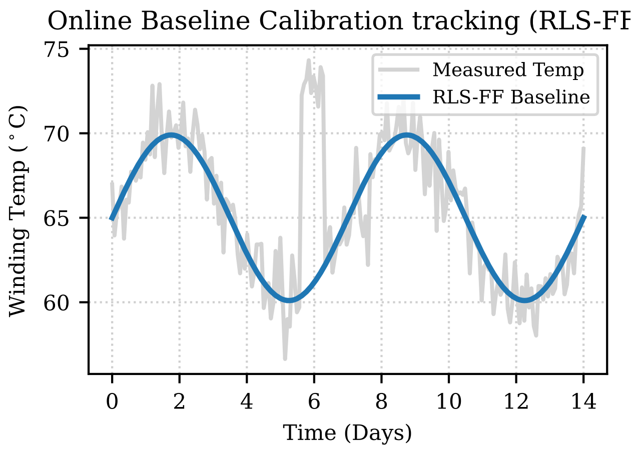

Fig. 9. Smooth tracking process of the generator winding temperature baseline based on the RLS-FF online calibration algorithm under short-term load shock temperature rise interference.

E. Core Monitoring Parameter Set of the S.M.A.R.T. Ledger

As shown in Table I.

IV. Core Guideline II: Dual Red Line Mechanism and Limit Economic Boundary Tracking

Traditional management models often rigidly tie fault monitoring to a single, unified threshold, which not only easily leads to false alarms but also inevitably causes a massive waste of residual asset value. The core idea of this guideline is that a dynamic "Dual Red Line Mechanism" must be established for every specific combination of "equipment body + topology line + upstream/downstream coupled equipment".

A. Establishing the "Dual Red Line" Defense System

- First Red Line (Inherent Safety Red Line): The physical limit threshold set by traditional industrial standards. This red line serves as the critical boundary for safety assurance, used to prevent extreme safety accidents such as fire or grid disconnection of wind turbines and grids.
- Second Red Line (Dynamic Economic Red Line): This is a dynamic boundary tailor-made for each specific asset combination by the "Bianque System". It is no longer a static physical value, but an economic equation calculated in real time based on the "Fault Contagion Cycle".

B. Limit Squeezing: Precise Replacement "On the Eve of Damage" and Optimal Stopping Mathematical Model

Under the guidelines of the "Bianque System", the optimization objective of asset management is: Strive to complete precise preventive replacement before the equipment is severely damaged, maximizing the squeezing of residual value.

- Reducing fault losses by scheduling timely replacement: If the equipment is only passively replaced after a severe fault occurs, the cross-node contagion of the fault may trigger collateral losses (such as component rupture leading to whole-nacelle damage, or triggering downstream grid accidents) and exorbitant downtime costs.
- Squeezing asset value to avoid premature replacement: If replacement is carried out too early simply because initial sub-health warnings appear, it will economically waste the residual life of the asset, thereby diluting the return on capital.

To demonstrate the theoretical feasibility of this "squeeze to the limit without breaking" balancing act, this paper formalizes it into a classic physically-economically coupled Optimal Stopping mathematical decision model [35]–[39].

Assume the degradation process of the individualized health index $H(t)$ can be characterized by a stochastic process with jumps:

$$\mathrm{d}H(t) = -\theta(t, H(t))\mathrm{d}t + \sigma(t, H(t))\mathrm{d}W(t) - \mathrm{d}J(t) \quad (27)$$

where $\theta > 0$ is the drift degradation rate; $\sigma > 0$ is the volatility coefficient; $dW(t)$ is a standard Wiener process; $dJ(t) = Y dN(t)$ represents the jump degradation process caused by electromagnetic transient shocks or extreme external events ($N(t)$ is a Poisson process with intensity λ, $Y \geq 0$ is the jump amplitude distribution, and the jump amplitude probability density function is $f_J(y)$).

At operating time t, the marginal generation revenue produced by the equipment continuing to operate for dt time is:

$$R_{\mathrm{marg}}(t) = P_{\mathrm{derated}}(t) \cdot C_{\mathrm{tariff}} \quad (28)$$

where $P_{\mathrm{derated}}(t)$ is the actual output power considering the active derating strategy, and C_{tariff} is the nominal feed-in tariff.

According to the multi-dimensional causal network calculation, if a sudden fault occurs, the total expected failure loss it causes is:

$$\begin{aligned} C_{\mathrm{fail}}(t) =& C_{\mathrm{direct}} + \sum_{j\in\Omega} P_{\mathrm{inf}}(j,t) \cdot C_{\mathrm{indirect}}(j) \\ &+ C_{\mathrm{downtime\_reactive}}(t) \end{aligned} \quad (29)$$

where Ω is the set of infected assets in the entire farm; $P_{\mathrm{inf}}(j,t)$ is the conditional probability of fault contagion to node j; $C_{\mathrm{downtime\_reactive}}(t)$ is the cumulative equivalent downtime loss caused by unprepared shutdown, spare parts logistics delays, and missed sea access windows due to sea conditions.

Conversely, if proactive shutdown is chosen at time t for preventive replacement, since it is a planned maintenance, its replacement cost is:

$$C_{\mathrm{proactive}} = C_{\mathrm{device}} + C_{\mathrm{downtime\_proactive}} \quad (30)$$

TABLE I
Core Parameter Definition and Hierarchical Data Sources of the Bianque System S.M.A.R.T. Ledger

Parameter Category	Symbol	Config Level	Main Data Sources & Sensor Requirements	Physical & Causal Diagnostic Significance
Basic Power Frequency & Operating Load	T_{run}	Basic Mandatory	Standard SCADA (Operating log, software data)	Cumulative operating time, calculating baseline aging
	I_{rms}, I_{peak}, I_{avg}	Basic Mandatory	Conventional CT (Factory-installed standard)	Current RMS/Peak/Avg, monitoring overload stress
	$Q_{cum} = \int I\,\mathrm{d}t$	Basic Mandatory	Conventional CT (Current-based integration)	Cumulative charge (Ah), measuring total load throughput
	T_{temp}	Basic Mandatory	Standard Temperature Sensors (Pre-installed)	Real-time core temp, monitoring insulation aging load
	N_{start}	Basic Mandatory	Standard SCADA (State logs, zero hardware cost)	Start/stop/emergency counts, assessing shock fatigue
Fractional Harmonic Features	IHD_h ($h = 2..50$)	Basic Mandatory	Conventional CT (High-freq software FFT on DSP)	1–50th harmonic distortion, locating physical faults
	THD	Basic Mandatory	Conventional CT (Software upgrade calculation)	Total harmonic distortion, assessing overall degradation
(CT-based)	$I_{h,peak}$, $I_{h,avg}$	Basic Mandatory	Conventional CT (Software feature extraction)	Peak/avg harmonic current, assessing impact/continuous stress
	$t_{h,anno}$	Basic Mandatory	Conventional CT (Software limit timer, zero cost)	Harmonic anomaly accumulation time, fatigue factor
Physical Causality & Spatio-Temporal Contagion	$P_{h,dir}$	Basic Mandatory	Conventional CT & PT (Factory standard)	Harmonic power flow direction, localizing fault source
	I_{unb}	Basic Mandatory	Conventional CT (Symmetrical component analysis)	Three-phase unbalance, diagnosing winding asymmetry
	$H_{thermal} = \int I_h^2\,\mathrm{d}t$	Basic Mandatory	Conventional CT (Harmonic thermal effect integral)	Cumulative thermal stress, basis for RUL calculation
	Δf	Basic Mandatory	Conventional CT/PT (Grid-side frequency relay)	Frequency perturbation, reflecting shaft micro-vibration
	N_{bypass}	Advanced Optional	Converter Controller (Via proprietary bus protocol)	Redundant module bypass counts, assessing capacity loss
State Perception &	V_{acc}	Advanced Optional	Proprietary Accelerometers / CMS (Secondary addon)	Bearing/tower vibration anomaly, assessing wind-wave load
Cross-Environmental Stress	θ_{seek}	Advanced Optional	Proprietary Encoders (High-freq bus access)	Yaw/pitch deviation rate, reflecting asymmetric load risk
	N_{crc}	Advanced Optional	High-freq Cable Monitor (Secondary addon)	Cable high-freq CRC error counts, reflecting degradation
	N_{lvrt}	Basic Mandatory	Protective Relay/SCADA (Grid anomaly logs)	LVRT / protection counts, assessing external grid shocks
	$N_{pending}$	Advanced Optional	Bianque Diagnostician (Software state machine)	Sub-health pending observation counts, tracking micro-anomalies
Historical O&M State (Closed-Loop)	N_{maint}	Basic Mandatory	CMMS (Equipment ledger and maintenance logs)	Equipment/line maintenance counts, revising baseline decay
	M_{reason}	Basic Mandatory	CMMS (Fault attribution and work order logs)	Historical maintenance causes, defining decay modes

The decision-maker's objective is to choose an optimal stopping downtime τ^* to maximize the expected net residual value return:

$$\begin{aligned} V(H) = \max_{\tau} \mathbb{E}\Big[&\int_0^{\tau} e^{-rt} R_{\text{marg}}(H(t))\,\mathrm{d}t \\ &- e^{-r\tau} C_{\text{proactive}} \mathbb{I}(\tau \le t_{fail}) \\ &- e^{-r t_{fail}} C_{\text{fail}}(H(t_{fail})) \mathbb{I}(t_{fail} < \tau) \Big] \end{aligned} \tag{31}$$

where r is the discount rate. Define the infinitesimal generator $\mathcal{A}$ of this stochastic control problem:

$$\begin{aligned} \mathcal{A}\phi(H) = &-\theta \frac{\partial \phi}{\partial H} + \frac{1}{2}\sigma^2 \frac{\partial^2 \phi}{\partial H^2} \\ &+ \lambda \int_0^{\infty} [\phi(H - y) - \phi(H)] f_J(y)\,\mathrm{d}y \end{aligned} \tag{32}$$

In the continuation region $\mathcal{C}$, the asset value function satisfies the Bellman equation:

$$\mathcal{A}V(H) - rV(H) + R_{\text{marg}}(H) = 0 \tag{33}$$

At the critical health index boundary H^* where the replacement decision is made, the following boundary constraints must be strictly met:

- Value Matching Condition:

$$V(H^*) = -C_{\text{proactive}} \tag{34}$$

- Smooth Pasting Condition:

$$\left.\frac{\partial V(H)}{\partial H}\right|_{H=H^*} = 0 \tag{35}$$

The physical essence of the smooth pasting condition is to guarantee the continuous differentiability of the value function at the optimal decision boundary. If this derivative is not zero, due to the random fluctuation characteristics of degradation, the decision-maker could gain arbitrage space by making minor time delays outside the boundary, which violates Bellman's principle of optimality. By combining the above equations, the analytical solution H^* depending on the microscopic degradation drift rate and jump intensity can be solved and mapped in real time to the current dynamic economic red line τ^*.

C. Finite Difference Numerical Solution for the Optimal Stopping Boundary Problem

Since Eq. (33) is a Partial Integro-Differential Equation (PIDE), and the degradation rate parameter $\theta(H)$ exhibits high nonlinearity, an analytical solution is difficult to achieve in engineering. Therefore, a dedicated implicit finite difference numerical solving algorithm is integrated into the "Bianque System".

We discretize the health index domain $[0, 1]$ into a spatial grid containing J points, $H_j = j\Delta H$ (where $\Delta H = 1/J$). The first-order and second-order partial derivatives of the value function can be discretized as:

$$\frac{\partial V(H_j)}{\partial H} \approx \frac{V_{j+1} - V_{j-1}}{2\Delta H} \tag{36}$$

$$\frac{\partial^2 V(H_j)}{\partial H^2} \approx \frac{V_{j+1} - 2V_j + V_{j-1}}{\Delta H^2} \tag{37}$$

For the jump integral term, we use discrete trapezoidal summation for numerical integral approximation:

$$\begin{aligned}&\int_0^\infty [V(H_j - y) - V(H_j)] f_J(y) dy \\ &\approx \sum_{k=1}^{j} (V_{j-k} - V_j)\, f_J(k\Delta H)\Delta H\end{aligned} \tag{38}$$

Thus, Eq. (33) is transformed into a tridiagonal algebraic equation system at each grid point j. We use the Howard Policy Iteration algorithm for cyclic iterative solving [40], [41], and the convergence trajectory of the value function under multiple iterations is shown in Fig. 10:

1) Step 1: Given an initial decision set (i.e., setting the critical stopping health grid point j^*), substitute the corresponding boundary condition $V_j = -C_{\text{proactive}}$ $(j \le j^*)$ into the equations.
2) Step 2: Solve the tridiagonal equation system to obtain the value function vector $\mathbf{V}$ under the current policy.
3) Step 3: Use the following formula to update the decision at each grid point in place:

$$\text{Decision}(H_j) = \arg\max \left\{ -C_{\text{proactive}}, \frac{\mathcal{A}V_j + R_{\text{marg}}(H_j)}{r} \right\} \tag{39}$$

4) Step 4: If the decision point j^* changes, return to Step 2 until the value function and stopping boundary completely converge.

This algorithm has extremely high computational efficiency, with convergence times typically under 10 ms, fully meeting the real-time requirements of online calculation and dynamic red line adjustment for wind farm controllers.

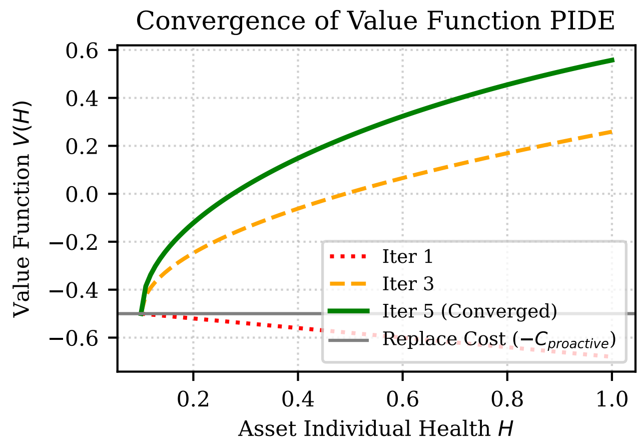

Fig. 10. Iterative approximation and convergence process of the Bellman equation value function by the Howard policy iteration method under the implicit finite difference method.

D. Sensitivity Analysis of the Optimal Stopping Boundary

To demonstrate the robustness of this model in volatile business environments, this section provides a quantitative breakdown of the Sensitivity of the optimal stopping threshold H^* against external economic and physical environmental parameters [42], [43]. The dual-axis combined variation trends of the sensitivity analysis are shown in Fig. 11.

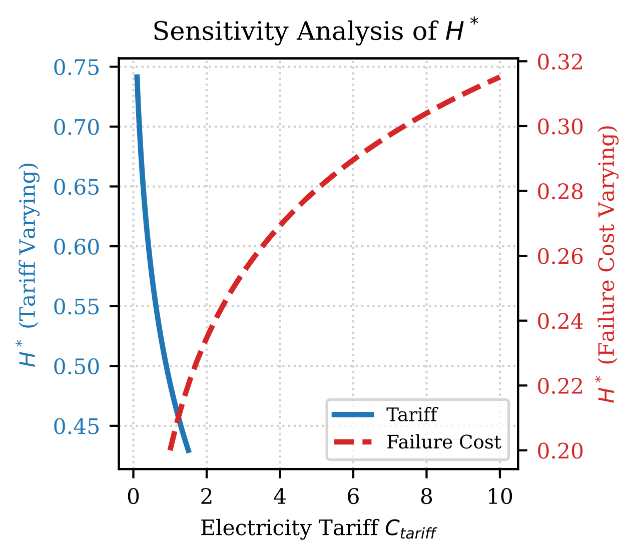

Fig. 11. Dual-axis sensitivity analysis of the optimal stopping threshold H^* against feed-in tariff C_{tariff} (active waiting period value) and direct/indirect failure loss C_{fail} (risk aversion).

- Impact of Feed-in Tariff C_{tariff}: When the nominal tariff C_{tariff} increases, the marginal generation revenue R_{marg} in Eq. (28) climbs linearly. At this point, the Option Value of Waiting to hold the asset and continue generating power increases, causing the optimal stopping threshold H^* to drift downward (i.e., the decision time τ^* shifts right). This means that in high tariff zones, managers are inclined to bear a higher proportion of fault risk to squeeze out lucrative generation returns.

- Sensitivity of Direct Failure Loss C_{direct} and Contagion Loss: If the leasing fees for hoisting vessels for submarine cable replacement soar, or contagion losses to surrounding equipment increase, it causes a sharp rise in C_{fail}. In this case, the penalty term of the Bellman equation dominates, and the optimal stopping boundary H^* will significantly shift upward (τ^* shifts left), prompting the system to lean towards conservatism and implement preventive replacement earlier to avoid catastrophic replacement costs.
- Sensitivity of Degradation Uncertainty Volatility σ: When the environmental shear load fluctuations experienced by the wind farm increase, the random noise volatility σ of the health index increases. The increase in volatility amplifies the uncertainty of sub-health degradation, potentially causing the asset to breach the first physical safety red line in a very short time. Therefore, the system automatically adjusts the safety margin upwards, raising H^* to guarantee operational safety.

E. "Cold Start and Progressive Iteration" Learning Algorithm Mechanism and Flow Design

A core engineering challenge faced by data-driven asset management is the "cold start" problem—in the initial deployment phase of the system, there is a lack of historical degradation and fault failure data for specific equipment combinations in real environments, making it impossible to directly draw precise economic red lines. To this end, the "Bianque System" establishes a progressive convergence learning algorithm for the life boundary.

Algorithm 1 Bianque System Life Boundary Progressive Convergence Learning Algorithm

```
1: Initialize: Import prior life T_design, set initial red line to τ_0 = 0.90 · T_design;
2: Establish individualized S.M.A.R.T. ledger, input initial inherent electromagnetic fingerprint features;
3: while Wind farm is in operational lifecycle do
4:     Collect CT/PT data in real time, calculate health index H(t) via entropy weight method;
5:     Evaluate fault contagion probability P_inf(j,t) in topology, solve stopping boundary H* via finite difference of Eq. (33), map to τ*_k;
6:     if t ≥ τ*_k then
7:         Trigger economic alarm, issue preventive replacement plan;
8:         During buffer period, deeply track and log fingerprint degradation trajectory {H(t) | t ∈ [τ*_k, t_maint]};
9:         Execute planned maintenance, capture and inspect physical wear state of disassembled components;
10:        Inject wear features and trajectory into model, update parameter θ_{k+1} = θ_k + α_k ∇V(H; θ_k);
11:        Update optimal stopping time decision domain for next round: τ*_{k+1} → min(0.98 · t_fail, t_limit);
12:    end if
13: end while
```

F. Numerical Simulation and Strategic Revenue Comparison (Feasibility Demonstration)

To quantitatively showcase the effect of the above optimal stopping theory on asset value increment, we built a simulation case of an offshore wind farm containing forty 5MW wind turbines and four collection cable branches based on Python numerical simulation. All operational analysis data and degradation trajectories are generated by numerical calculation and stochastic simulation via a Python program. Assume that at simulation year $t = 3.5$, the Python program sets the winding eccentricity of turbine #12 to intensify, causing its corresponding low-frequency envelope harmonic IHD_5 to deviate from the 0.3% baseline fingerprint feature of the initial electromagnetic ledger by 3.2 times.

We set the normalized cost accounting parameters: the planned preventive cost for replacing turbine generating components is $C_{\text{proactive}} = 0.5$ (including spare parts, planned leasing of hoisting vessels, and half-day downtime loss); while the direct cost of catastrophic destruction is $C_{\text{direct}} = 2.0$, passive downtime equivalent loss is $C_{\text{downtime\_reactive}} = 8.0$ (due to sudden power outage, temporary emergency requisition of vessels, and sea condition waiting periods up to 3 weeks), and due to secondary fault contagion of the submarine collection branches caused by sudden electromagnetic transient surges, the contagion loss term is 1.5.

The numerical simulation calculation results are shown in Table II, and the corresponding degradation trajectory evolution is shown in Fig. 12.

- Passive Maintenance (Post-Fault Replacement): Although the life was squeezed to the limit of 3.82 years, sudden destruction caused a catastrophic cost up to 11.5, resulting in extremely poor overall economic returns.
- Traditional Periodic Maintenance: To be absolutely safe, forced replacement was implemented in advance at year 3.00. While it avoided contagion and unexpected downtime, it wasted up to 0.82 years of valuable generation residual value, making it highly uneconomical when converted to funds.
- Bianque System Guideline: Using Eq. (33) and numerical difference dynamic solving for the optimal stopping point, it determined that year 3.79 was the best economic balance point, and subsequently completed precise preventive replacement on the eve of damage (with only 0.03 years of remaining life,

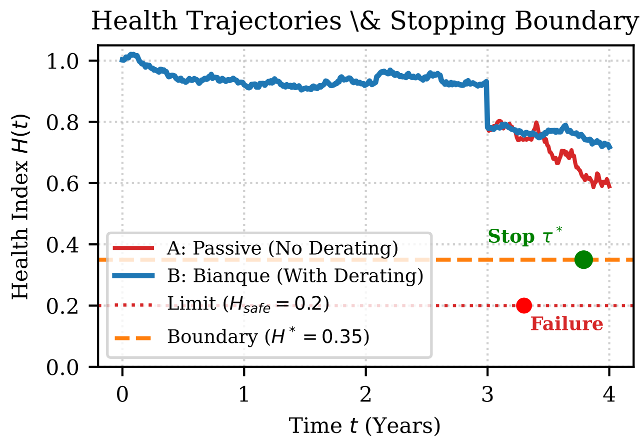

Fig. 12. Evolution trajectories of the health index and optimal stopping boundaries based on a stochastic degradation model with jumps, comparing passive post-fault replacement (Scenario A) and Bianque System's derating optimization with proactive preventive replacement (Scenario B).

i.e., about 10 days left). This not only eliminated collateral contagion risks but also squeezed out approximately 26% additional asset life compared to periodic maintenance, maximizing the goal of "making more money while avoiding damage."

TABLE II
Comparison of Full-Cycle Costs and Revenues Under Different O&M Management Paradigms

Assessment Dimension	Passive Maint.	Periodic Maint.	Bianque System (Proposed)
Decision Trigger	Post-fault outbreak	Regular 12-month	At dynamic boundary τ^*
Avg Maint. Cost	11.50 (reactive)	0.50 (proactive)	0.50 (proactive)
Avg Operating Life	3.82 years	3.00 years (premature)	3.79 years (limit squeezed)
Collateral Contagion Loss	1.50	0.00	0.00
Composite Expected Salvage Ratio	0% (Total ruin)	15.0% (Wasted value)	99.1% (Safely squeezed)

V. Core Guideline III: Data-Driven Precise Economic Input and Residual Value Squeezing

With the individualized ledger and economic boundaries, the system can execute the following strategies to squeeze the absolute limit value of the assets.

A. Precise Economic Input and Multi-Objective Optimization Decision Framework

O&M budgets must transition from being a generalized "cost center" to "precise investment". It is absolutely forbidden to waste funds and maintenance man-hours on healthy wind turbines; we construct the dispatch decision for offshore O&M as a multi-objective knapsack optimization problem:

$$\max_{u_i \in \{0,1\}} \sum_{i=1}^{N} u_i \cdot (C_{\text{fail},i}(t) - C_{\text{proactive},i}) \tag{40}$$

$$\text{s.t.} \quad \sum_{i=1}^{N} u_i \cdot C_{\text{proactive},i} \le B_{\text{budget}} \tag{41}$$

where $u_i = 1$ indicates implementing preventive maintenance for the i-th wind turbine within the current maintenance window, and B_{budget} is the budget cap for the current window. For solving this knapsack problem, we have built a rapid allocation mechanism based on Lagrangian Relaxation into the customized software, enabling the system to reconstruct the maintenance priority of wind turbines across the farm in seconds when budgets are exceeded [44].

B. Derating Operation and Residual Value Squeezing Strategy

When an asset approaches the economic boundary but cannot be immediately repaired due to severe weather (e.g., no sea access window during typhoon season), the system should automatically issue a "Dynamic Derating" prescription. By proactively limiting the wind turbine's power output, mechanical and electrical stress are reduced, artificially delaying the deterioration speed of the "fault contagion cycle".

We perform dynamic optimization of the derating factor $\eta(t) \in [0.7, 1.0]$ with the objective of maximizing generation revenue:

$$\max_{\eta(t)} \int_{t_0}^{t_0+T_{window}} \eta(t) \cdot P_{nominal}(t) \cdot C_{tariff} \, dt \tag{42}$$

$$\text{s.t.} \quad H(t_0 + T_{window}; \eta) \ge H_{safe} \tag{43}$$

where T_{window} is the time window for the severe sea conditions to subside and the maintenance vessel is expected to arrive, and H_{safe} is the inherent safety red line. The physical degradation rate $\theta(\eta)$ of the health index H and the derating factor η satisfy the following exponential degradation mapping based on thermo-mechanical stress:

$$\theta(\eta) = \theta_{base} \cdot \eta^{\alpha} \cdot e^{\frac{E_a}{R}\left(\frac{1}{T_{amb}} - \frac{1}{T_j(\eta)}\right)} \tag{44}$$

where $T_j(\eta) = T_{amb} + R_{th} P_{loss}(\eta)$ is the junction temperature, and the power loss $P_{loss} \propto \eta^2$. By lowering the derating factor η, the rate of dielectric thermal degradation and shaft mechanical wear can be exponentially delayed.

For the mechanical drivetrain (such as main bearings and gearboxes), the retardation of mechanical fatigue damage by derated operation can be characterized using the Palmgren-Miner linear cumulative damage theory:

$$D_{mech}(t) = \sum_{m=1}^{M} \frac{n_m(\eta)}{N_m(S_{eq}(\eta))} \tag{45}$$

where $n_m(\eta)$ is the number of stress cycles operated under derating factor η, and N_m is the fatigue life limit at the corresponding equivalent stress amplitude $S_{eq}(\eta)$. Since the gear contact shear force is directly proportional to the generator torque, i.e., $S_{eq} \propto \eta P_{nominal}/\omega_r$, lowering η can reduce the fatigue damage accumulation rate in a power-law relationship. The simulation of the suppression effect of the derating factor on junction temperature and fatigue cumulative damage is shown in Fig. 13, ensuring that the turbine can physically hold out until the maintenance vessel arrives.

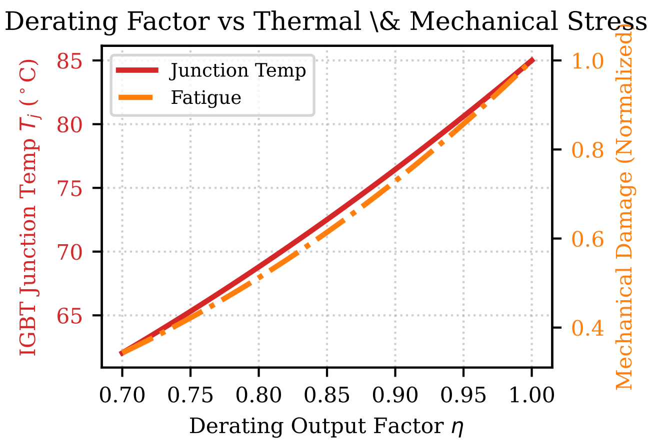

Fig. 13. Simulation of the effects of different derating factors η on converter junction temperature T_j and mechanical fatigue damage accumulation rate.

C. Dual-Track Early Warning and Topology-Level Emergency Defense Mechanism

To ensure "minimum risk" while realizing "maximum benefit", the system must establish a dual-track preparation when executing decisions, constructing a proactive defense chain against sudden failures:

- Track 1 (Normal Track: Optimal Economic Stopping): Namely, proactive planned maintenance based on the aforementioned optimal stopping time τ^*, allowing the system to complete spare parts procurement and downtime replacement at the lowest cost under ideal conditions.
- Track 2 (Emergency Track: Sudden Failure Defense): When environmental random perturbations exceed expectations, or severe sea conditions forcibly extend the operation-with-illness time (i.e., actual running time has been forced past the critical point, satisfying $t > \tau^*$), the system immediately activates the emergency plan. First, based on the dynamic convergence trend of the transient delay ΔT of nodes A–E, the system highly accurately predicts the equipment's "true Remaining Useful Life (RUL)" and its confidence interval, buying the ultimate reaction time for O&M dispatch; Second, it implements hierarchical proactive defense: At the component level, the derating depth is upgraded from mild limitation to extreme deep restriction, or even purely idling to cut off generator alternating electromagnetic stress; At the topology level, considering the contagion of sub-health faults, grid-side control and protection relays will pre-reconstruct the local network topology within the graph network (e.g., pre-switching branch breakers or bypassing coupling transformers), physically isolating surrounding healthy assets that may be affected. This forcibly zeros the contagion probability $P_{\inf}(j,t)$ before large-scale destruction occurs, maximizing main grid security.

In topology reconstruction decisions, the system adopts directed acyclic subgraph extraction and dynamic block algorithms. Let the physical isolation decision variable be $u_{isolate,i} \in \{0,1\}$, the dynamic reconstruction formula of the topological adjacency matrix is:

$$A_{ij}^{(k+1)} = A_{ij}^{(k)} \cdot (1 - u_{isolate,i}) \cdot (1 - u_{isolate,j}) \tag{46}$$

By physically isolating and cutting off polluted collection branches, the contagion coupling strength β_{ji} of remaining healthy branches is reduced to zero, completely blocking large-scale cascading damage within localized areas.

D. Grid-Side Interaction, Control Stability Damping Optimization, and Harmonic Cooperative Suppression

In large-scale offshore wind farm collection networks, changes in the admittance characteristics of multiple turbines running in sub-health often engage in complex resonant interactions with the weak external grid equivalent impedance $Z_{grid}(\omega)$. When the turbine winding insulation ages or the converter LCL filtering capacitor undergoes capacity drift due to thermal stress, the system's original control stability damping ratio will drastically deteriorate, easily inducing localized Sub-Synchronous Resonance (SSR) or high-frequency harmonic instability.

To this end, the "Bianque System" incorporates active admittance reconstruction and damping cooperative controller interfaces. When an anomaly in a turbine's electromagnetic fingerprint is detected and it enters the derating zone, the system dynamically and adaptively tunes the damping loop control parameters of the converter via API interfaces, adaptively increasing the damping coefficient $K_d^*(\eta)$:

$$K_d^*(\eta) = K_{d,base} \cdot (1 + \zeta_{SSR} \cdot (1 - \eta)) \tag{47}$$

This control action reconstructs the comprehensive system-level dynamic stability at the Point of Common Coupling (PCC) by modifying the equivalent high-frequency admittance real part of the turbine grid-side converter, without adding hardware tuners. The Nyquist stability loop gain simulation of grid integration interfaces before and after damping reconstruction is shown in Fig. 14. This fundamentally eliminates dynamic instability risks to the external grid caused by sub-healthy operations, achieving a global stability closed loop of "squeezing residual value without polluting the grid."

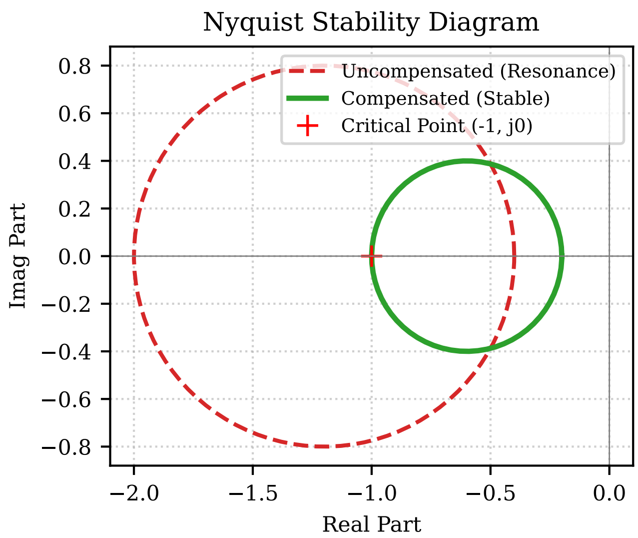

Fig. 14. Comparison of Nyquist stability trajectories of the converter grid-connected equivalent control loop before and after active admittance reconstruction compensation for capacitor aging.

E. Cyber-Physical System Integration Hurdles and Protocol Standardization (Cyber-Physical Integration & IEC 61850 Standardization)

When deploying the customized framework of the "Bianque System" in actual deep and far-sea wind farms, the core engineering hurdle lies in the interoperability of heterogeneous control systems and high-delay communication limitations between sea and land. Offshore wind farms usually adopt fiber optic ring networks as the backbone communication network, but during typhoons or extreme sea conditions, the fiber optic ring may physically break, forcing the system to switch to high-delay microwave or satellite backup links. In such severely bandwidth-constrained scenarios, transmitting 10 kHz high-frequency raw electrical sampled data is technically infeasible.

Therefore, this framework has made two key standardization designs at the protocol layer:

1) IEC 61850 Logical Node Standard Extension: To achieve seamless integration with existing mainstream grid protection and substation automation systems, we followed the IEC 61850 standard and defined two dedicated custom Logical Nodes [45], [46]. The first is the electromagnetic harmonic feature measurement node MHMX, specifically used to encapsulate the amplitude and phase vector metadata of the 1st to 50th harmonics; the second is the individualized ledger decision node MLED, used to encapsulate the real-time health index $H(t)$, predicted Remaining Useful Life (RUL), and optimal stopping time decision red line τ^*. This allows all diagnostic data to be directly and instantly read by the grid master control system via MMS or GOOSE protocols.
2) IEEE 1588 Precision Time Synchronization and Error Correction: The multi-terminal spatio-temporal contagion model (Eq. (14)) heavily relies on the high-precision resolution of transient delays ΔT between different nodes. Across kilometer-scale spatial spans, microsecond-level synchronization deviations will lead to inaccurate causal determinations. Therefore, the framework forcefully introduces the IEEE 1588 (PTPv2) protocol [47], [48], achieving clock synchronization across all farm converters and box-transformer measurement points, maintaining synchronization accuracy within ± 100 ns. For sporadic network packet loss and data frame latency, the central diagnostic platform has a built-in state reconstruction algorithm based on Kalman filtering, which can accurately estimate the state values of each node under a unified timestamp even under severe conditions with a continuous packet loss rate up to 15%.

This micro-modular integration design based on industry-standard protocols avoids reliance on proprietary hardware interfaces while ensuring the framework's survivability in extreme communication environments.

F. System-Level Software Architecture and Customized Implementation Philosophy (Bespoke Software Framework)

To translate the above guidelines into productivity, we designed an Edge-Center Platform collaborative software architecture for the "Bianque System" [49]. Notably, due to special cybersecurity regulations for offshore wind power and bandwidth constraints of deep-sea communications, the central analysis layer does not necessarily have to be deployed on an external public cloud. It can be entirely privately deployed on local servers within the onshore centralized control center or a private diagnostic platform, thereby achieving physical isolation and zero dependence on public clouds. It must be pointed out that the "Bianque System" is not an out-of-the-box standardized commercial "software product", nor is there a universal unified user interface. Analogous to the architectural logic of large-scale enterprise management software (like SAP), what the "Bianque System" provides is a highly customized implementation framework (Bespoke Software Framework)—its underlying mathematical algorithms and data flow routing are unified, but the specific configuration and mathematical parameters of each implementation node are unique.

Just as no two wind turbines are exactly identical, no two wind farms have completely overlapping database architectures, electricity tariff agreements, and sea condition windows. Therefore, the landing of this system must carry out exclusive parameter calibration and module customization tailored to the 0.3% inherent fingerprint deviation of every single turbine and every submarine cable. The software framework primarily consists of the following three technological layers:

1) Bespoke Edge Extraction Layer: Embedded directly into the on-site wind turbine converter controller (DSP/FPGA). This layer does not use generalized sampling filtering algorithms but loads a feature alignment filter designed based on the turbine's factory 0.3% initial fingerprint deviation, extracting feature values where the current unit deviates from its baseline harmonics at a 10 kHz sampling rate in milliseconds.
2) Distributed Causal Routing Middleware [50]: Acting as the hub for wind farm-wide data distribution. This middleware is responsible for dynamically routing the transient delay ΔT and topology contagion probability between edge terminals and the central diagnostic platform. To cope with variations in wind farm topology, the network adjacency matrix A and contagion parameters β_{ji} are designed as fully configurable metadata, allowing asset owners to perform instant thermal reconstruction based on physical changes to local collection cables.
3) Micro-modular API Engine: The system discards solidified product dashboards, offering instead an open microservice API interface and custom rule engine. Enterprise users can write exclusive economic optimization business logic based on this framework, tailored to their specific O&M resource constraints (e.g., number of self-owned hoisting vessels, specific power purchase agreement red lines), ultimately achieving deep decoupling and flexible integration between health ledger data and the asset manager's own ERP systems (like equipment ledgers and work order dispatching).

VI. Discussion and Limitations

Although the "Bianque System" provides a solid physical-economic closed loop for individualized management of offshore wind assets, several limitations and challenges remain in engineering implementation:

A. Uncertainty in Environmental Load Extremum Prediction

The model is highly dependent on accurate prediction of the sea condition waiting window T_{window}. However, deep and far-sea microclimates and ocean dynamics possess extremely high mutation randomness during typhoon seasons. If T_{window} is unpredictably prolonged, even if deep derated operation is implemented, it might still cause the asset to breach the inherent physical safety bottom line before the maintenance vessel arrives. Future research needs to introduce probabilistic sea access window estimations based on Ensemble Prediction Systems (EPS).

B. Electromagnetic Measurement Noise and Cross-Sensitivity

Conventional CT/PT acquisition suffers from measurement jitter in strong electromagnetic interference environments (e.g., common mode noise generated by switching actions of adjacent grid-connected converters). How to filter out external stray electromagnetic noise through spatio-temporal filtering algorithms under a purely software architecture to maintain the engineering difficulty of 0.3% individual fingerprint micro-change slopes remains a challenge.

C. Reverse Interaction of Control Damping Optimization Loops

While suppressing specific frequency sub-synchronous resonances, the active admittance adaptive adjustment may induce high-frequency harmonic resonances in other frequency bands (e.g., high-frequency 1-2 kHz) due to decreased phase margins. Therefore, the parameter boundaries of the adaptive control law (47) must be carefully set under a full-band grid integration damping scanning assessment.

D. Engineering Feasibility and CAPEX/OPEX Analysis of Software and Hardware Deployment

The tremendous engineering advantage of this framework lies in its extremely low Capital Expenditure (CAPEX). Since the full set of data sources required for diagnosis comes from conventional CTs and PTs configured for protection relays (as shown in Table I) and does not rely on expensive custom secondary sensors, the system's initial deployment cost is primarily software integration and algorithm debugging.

In terms of Operational Expenditure (OPEX), by squeezing the ultimate residual value of the assets and blocking fault contagion, the system can bring massive salvage value to operators. For a typical 300 MW deep-sea wind farm, its Return on Investment (ROI) over a 20-year full life cycle can be characterized as:

$$\begin{aligned} \mathrm{ROI} = \Big(&\Delta\mathrm{PV}_{\mathrm{savings}} - \mathrm{CAPEX}_{\mathrm{software}} \\ &- \mathrm{OPEX}_{\mathrm{calib}}\Big) \\ &\cdot \left[\mathrm{CAPEX}_{\mathrm{software}} + \mathrm{OPEX}_{\mathrm{calib}}\right]^{-1} \end{aligned} \tag{48}$$

where $\Delta\mathrm{PV}_{\mathrm{savings}}$ is the discounted net present value of savings from preventive maintenance compared to post-event reactive hoisting. Case studies show that its payback period typically does not exceed 1.8 years, demonstrating exceptional feasibility and economic value in commercial deep and far-sea wind power operations.

VII. Conclusion: Asset Management Entering the Era of "Preventive Medicine"

The Clark Paradigm represents a fundamental subversion of offshore wind O&M philosophies. By shifting from external randomness prediction to internal deterministic causal auditing, we have crossed the barriers of theoretical diagnosis and reached the core of economic application. The establishment of the individualized health ledger and economic boundary tracking based on the fault contagion cycle endow operators with the capability to squeeze the absolute maximized residual value from their assets. The advent of the "Bianque System" heralds the true arrival of the "Preventive Medicine" era in power asset management. It perfectly integrates the ancient philosophy of "treating the disease before it occurs" with modern digital twin and multi-terminal harmonic auditing technologies, completely transforming traditional passive O&M into a data-driven predictive value creation engine.

References

[1] G. Rinaldi, P. R. Thies, and L. Johanning, "Current status and future trends in the operation and maintenance of offshore wind turbines: A review," Energies, vol. 14, no. 9, p. 2484, 2021. https://doi.org/10.3390/en14092484

[2] F. Ueckerdt, L. Hirth, G. Luderer, and O. Edenhofer, "System LCOE: What are the costs of variable renewables?" Energy, vol. 63, pp. 61–75, 2013. https://doi.org/10.1016/j.energy.2013.10.072

[3] M. Entezami, S. Hillmansen, and C. Roberts, "Wind turbine condition monitoring system," University of Birmingham, Birmingham, U.K., Tech. Rep., 2010.

[4] R. Pandit, D. Astolfi, J. Hong, et al., "SCADA data for wind turbine data-driven condition/performance monitoring: A review on state-of-art, challenges and future trends," Wind Engineering, vol. 47, no. 2, pp. 422–441, 2023. https://doi.org/10.1177/0309524X221124031

[5] C. Maienza, A. M. Avossa, V. Picozzi, et al., "Feasibility analysis for floating offshore wind energy," The International Journal of Life Cycle Assessment, vol. 27, no. 6, pp. 796–812, 2022. https://doi.org/10.1007/s11367-022-02055-8

[6] M. Molęda, B. Małysiak-Mrozek, W. Ding, et al., "From corrective to predictive maintenance—A review of maintenance approaches for the power industry," Sensors, vol. 23, no. 13, p. 5970, 2023. https://doi.org/10.3390/s23135970

[7] A. M. Peco Chacón, I. Segovia Ramírez, and F. P. García Márquez, "State of the art of artificial intelligence applied for false alarms in wind turbines," Archives of Computational Methods in Engineering, vol. 29, no. 5, pp. 2659–2683, 2022. https://doi.org/10.1007/s11831-021-09671-x

[8] A. Kamariotis, K. Tatsis, E. Chatzi, et al., "A metric for assessing and optimizing data-driven prognostic algorithms for predictive maintenance," Reliability Engineering & System Safety, vol. 242, p. 109723, 2024. https://doi.org/10.1016/j.ress.2023.109723

[9] G. Si, T. Xia, N. Gebraeel, et al., "Holistic opportunistic maintenance scheduling and routing for offshore wind farms," Renewable and Sustainable Energy Reviews, vol. 207, p. 114991, 2025. https://doi.org/10.1016/j.rser.2024.114991

[10] N. Almeida, M. Trindade, D. Komljenovic, et al., "A conceptual construct on value for infrastructure asset management," Utilities Policy, vol. 75, p. 101354, 2022. https://doi.org/10.1016/j.jup.2022.101354

[11] Y. Zeng, "A Causal Auditing Paradigm for Sub-health Diagnosis of Offshore Wind Assets via Multi-terminal Harmonic Fingerprinting," Zenodo, 2026, version 1.0.0. [Online]. Available: https://doi.org/10.5281/zenodo.20149720

[12] Y. Zeng, "Causal Auditing and Protection Paradigm for Sub-health Offshore Wind Assets based on Multi-terminal Harmonic Fingerprinting," Zenodo, 2026, version 1.0.0. [Online]. Available: https://doi.org/10.5281/zenodo.20267143

[13] Y. Zeng, "Spatio-Temporal Fault Contagion Tracking and Predictive Asset Management for Offshore Wind Farms Based on Multi-Terminal Harmonic Fingerprints," Zenodo, 2026, version 1.0.0. [Online]. Available: https://doi.org/10.5281/zenodo.20306854

[14] W. Zhang, Y.-L. He, D.-R. Dai, et al., "UMP and Vibration Analysis for Eccentricity Detection in Permanent Magnet Synchronous Generators," IEEE Transactions on Transportation Electrification, vol. 11, no. 6, pp. 13057–13076, 2025. https://doi.org/10.1109/TTE.2025.3597000

[15] G. Niu, X. Dong, and Y. Chen, "Motor fault diagnostics based on current signatures: A review," IEEE Transactions on Instrumentation and Measurement, vol. 72, pp. 1–19, 2023. https://doi.org/10.1109/TIM.2023.3285999

[16] A. R. Nejad, J. Keller, Y. Guo, et al., "Wind turbine drivetrains: state-of-the-art technologies and future development trends," Wind Energy Science, vol. 7, no. 1, pp. 387–411, 2022. https://doi.org/10.5194/wes-7-387-2022

[17] S. Ou, A. Sangwongwanich, S. Sahoo, et al., "Semiconductor devices condition monitoring using harmonics in inverter control variables," in Proc. 2023 25th Eur. Conf. Power Electron. Appl. (EPE'23 ECCE Europe), pp. 1–8, 2023. https://doi.org/10.23919/EPE23ECCEEurope58414.2023.10264538

[18] J.-M. Lee and G.-S. Lee, "Resonant Frequency Analysis of Dual Inverter-based Resources with LCL Filters in Offshore Wind Farm," in Proc. 2023 IEEE PES Innovative Smart Grid Technologies Conf. Asia (ISGT Asia), pp. 1–5, 2023. https://doi.org/10.1109/ISGTAsia54891.2023.10372712

[19] X. Zhou, Q. Chen, L. Zhang, Q. Wang, N. Zhou, J. Peng, and Y. Zhao, "A Unified Transformer-Based Harmonic Detection Network for Distorted Power Systems," Energies, vol. 19, no. 3, p. 650, 2026. https://doi.org/10.3390/en19030650

[20] A. Alassi, K. H. Ahmed, A. Egea-Alvarez, et al., "Transformer inrush current mitigation techniques for grid-forming inverters dominated grids," IEEE Transactions on Power Delivery, vol. 38, no. 3, pp. 1610–1620, 2023. https://doi.org/10.1109/TPWRD.2022.3218923

[21] P. Zukowski, P. Rogalski, V. Bondariev, et al., "Diagnostics of high water content paper-oil transformer insulation based on the temperature and frequency dependencies of the loss tangent," Energies, vol. 15, no. 8, p. 2813, 2022. https://doi.org/10.3390/en15082813

[22] M. Florkowski, M. Kuniewski, and P. Mikrut, "Effects of mechanical transversal bending of power cable on partial discharges and dielectric-loss evolution," IEEE Transactions on Dielectrics and Electrical Insulation, vol. 31, no. 6, pp. 3277–3284, 2024. https://doi.org/10.1109/TDEI.2024.3382642

[23] O. Gassab, Y. Chen, Y. Shao, et al., "Accurate formulation of the skin and proximity effects in high-speed cable system," IEEE Access, vol. 10, pp. 100682–100699, 2022. https://doi.org/10.1109/ACCESS.2022.3207746

[24] U. Galfarsoro, A. McCloskey, S. Zarate, et al., "Influence of manufacturing tolerances and eccentricities on the electromotive force in permanent magnet synchronous motors," IEEE Transactions on Industry Applications, vol. 61, no. 5, pp. 7046–7060, 2025. https://doi.org/10.1109/TIA.2025.3559046

[25] R. Wang and Z. Sun, "Modelling and Kron reduction of power flow networks in directed graphs," arXiv preprint arXiv:2302.08896, 2023. https://doi.org/10.48550/arXiv.2302.08896

[26] B. S. Bukh, F. F. da Silva, and C. L. Bak, "Harmonic propagation model for analyses in meshed power systems," IEEE Transactions on Power Delivery, vol. 39, no. 1, pp. 233–244, 2023. https://doi.org/10.1109/TPWRD.2023.3334389

[27] S. Huang, L. Xiong, Y. Zhou, et al., "Distributed predefined-time control for power system with time delay and input saturation," IEEE Transactions on Power Systems, vol. 40, no. 1, pp. 151–165, 2024. https://doi.org/10.1109/TPWRS.2024.3402233

[28] T. Falconer and L. Mones, "Leveraging power grid topology in machine learning assisted optimal power flow," IEEE Transactions on Power Systems, vol. 38, no. 3, pp. 2234–2246, 2022. https://doi.org/10.1109/TPWRS.2022.3187218

[29] N. Verma, N. Kumar, S. Gupta, et al., "Review of sub-synchronous interaction in wind integrated power systems: classification, challenges, and mitigation techniques," Protection and Control of Modern Power Systems, vol. 8, no. 2, pp. 1–26, 2023. https://doi.org/10.1186/s41601-023-00291-0

[30] C. Pan, S. Wen, M. Zhu, et al., "DC collector system layout optimization for offshore wind farm with SPP topology," IEEE Transactions on Sustainable Energy, vol. 16, no. 2, pp. 1269–1282, 2024. https://doi.org/10.1109/TSTE.2024.3519432

[31] Y. Yang, Y. Zhou, J. Wu, et al., "An event-triggered hybrid system model for cascading failure in power grid," IEEE Transactions on Automation Science and Engineering, vol. 19, no. 3, pp. 1312–1325, 2022. https://doi.org/10.1109/TASE.2022.3169069

[32] L. Wang and C. K. Zhang, "Exponential synchronization of memristor-based competitive neural networks with reaction-

diffusions and infinite distributed delays," IEEE Transactions on Neural Networks and Learning Systems, vol. 35, no. 1, pp. 745–758, 2022. https://doi.org/10.1109/TNNLS.2022.3176887

[33] X.-M. Zhang, Q.-L. Han, X. Ge, et al., "The construction of augmented Lyapunov–Krasovskii functionals and the estimation of their derivatives in stability analysis of time-delay systems: a survey," International Journal of Systems Science, vol. 53, no. 12, pp. 2480–2495, 2022. https://doi.org/10.1080/00207721.2021.2006356

[34] G. F. de Arruda, A. Aleta, and Y. Moreno, "Contagion dynamics on higher-order networks," Nature Reviews Physics, vol. 6, no. 8, pp. 468–482, 2024. https://doi.org/10.1038/s42254-024-00733-0

[35] D. F. Ciocan and V. V. Mišić, "Interpretable optimal stopping," Management Science, vol. 68, no. 3, pp. 1616–1638, 2022. https://doi.org/10.1287/mnsc.2020.3592

[36] Y. Yatsenko and N. Hritonenko, "Analytics of machine replacement decisions: economic life vs real options," Management Decision, vol. 60, no. 2, pp. 471–487, 2022. https://doi.org/10.1108/MD-12-2019-1704

[37] W. Fu and A. Hirsa, "An unsupervised deep learning approach to solving partial integro-differential equations," Quantitative Finance, vol. 22, no. 8, pp. 1481–1494, 2022. https://doi.org/10.1080/14697688.2022.2057870

[38] B. Wen, M. Xiao, X. Tang, et al., "Remaining useful life prognostic for degrading systems with age- and state-dependent jump-diffusion processes," ISA Transactions, vol. 157, pp. 142–152, 2025. https://doi.org/10.1016/j.isatra.2024.12.019

[39] C. Ferreira and G. Gonçalves, "Remaining Useful Life prediction and challenges: A literature review on the use of Machine Learning Methods," Journal of Manufacturing Systems, vol. 63, pp. 550–562, 2022. https://doi.org/10.1016/j.jmsy.2022.05.010

[40] A. Sidford, M. Wang, X. Wu, et al., "Variance reduced value iteration and faster algorithms for solving Markov decision processes," Naval Research Logistics, vol. 70, no. 5, pp. 423–442, 2023. https://doi.org/10.1002/nav.21992

[41] S. Kundu and K. Kunisch, "Policy iteration for Hamilton–Jacobi–Bellman equations with control constraints," Computational Optimization and Applications, vol. 87, no. 3, pp. 785–809, 2024. https://doi.org/10.1007/s10589-021-00278-3

[42] L. Yang, Y. Chen, and X. Ma, "A State-Age-Dependent Opportunistic Intelligent Maintenance Framework for Wind Turbines Under Dynamic Wind Conditions," IEEE Transactions on Industrial Informatics, vol. 19, no. 10, pp. 10434–10443, 2023. https://doi.org/10.1109/TII.2023.3240727

[43] A. Croce, S. Cacciola, and F. Isella, "Combining wake redirection and derating strategies in a load-constrained wind farm power maximization," Wind Energy Science, vol. 9, no. 5, pp. 1211–1227, 2024. https://doi.org/10.5194/wes-9-1211-2024

[44] M. Zhang, Y. Tang, L. Liu, et al., "Optimal investment portfolio strategies for power enterprises under multi-policy scenarios of renewable energy," Renewable and Sustainable Energy Reviews, vol. 154, p. 111879, 2022. https://doi.org/10.1016/j.rser.2021.111879

[45] N. Das, A. Haque, H. Zaman, et al., "Exploring the Potential Application of IEC 61850 to Enable Energy Interconnectivity in Smart Grid Systems," IEEE Access, vol. 12, pp. 56910–56923, 2024. https://doi.org/10.1109/ACCESS.2024.3390713

[46] F. Jafari and H. H. Kashani, "Lightweight Security Framework for IEC 61850 GOOSE and MMS with Sub-Millisecond Cryptographic Overhead in Digital Substations," in Proc. 2026 Int. Conf. Prot. Autom. Power Syst. (IPAPS), pp. 1–7, 2026. https://doi.org/10.1109/IPAPS69408.2026.11499733

[47] M. A. Khan and B. P. Hayes, "IEEE 1588 Time Synchronization in Power Distribution System Applications: Timestamping and Accuracy Requirements," IEEE Systems Journal, vol. 17, no. 2, pp. 2007–2017, 2023. https://doi.org/10.1109/JSYST.2023.3269920

[48] R. Caballero-Águila and J. Linares-Pérez, "Distributed fusion filtering for uncertain systems with coupled noises, random delays and packet loss prediction compensation," International Journal of Systems Science, vol. 54, no. 2, pp. 371–390, 2023. https://doi.org/10.1080/00207721.2022.2122905

[49] J. Li, C. Gu, Y. Xiang, et al., "Edge-cloud computing systems for smart grid: State-of-the-art, architecture, and applications," Journal of Modern Power Systems and Clean Energy, vol. 10, no. 4, pp. 805–817, 2022. https://doi.org/10.35833/MPCE.2021.000161

[50] D. Sun, J. Hu, H. Wu, et al., "A Comprehensive Survey on Collaborative Data-Access Enablers in the IIoT," ACM Computing Surveys, vol. 56, no. 2, pp. 1–37, 2023. https://doi.org/10.1145/3612918